

# Acoustic Emission Signal Propagation in Damaged Composite Structures

Markus G. R. Sause

University of Augsburg, Institute for Physics, Experimental Physics II, D-86135 Augsburg

## Abstract

Numerical studies were performed to investigate acoustic emission (AE) signal propagation in carbon fiber-reinforced plastic plates with internal damage. For the case of thin plates, Lamb waves are the dominating mode of propagation for ultrasonic waves. The interpretation of Lamb waves is one of the main challenges for valid source localization or identification procedures. Naturally, the lateral size and the thickness of the plate have a significant impact on the propagation behavior of guided waves. While these geometric dimensions can be understood as boundary conditions, distortions of wave patterns caused by internal discontinuities are more difficult to understand. During loading of a composite specimen, a variety of damage types can occur, that alter the properties of the composite. Although AE signals originate from the rapid microscopic displacement within the material, the interaction of the excited acoustic waves is not limited to microscopic dimensions. Due to the wavelength of the Lamb waves in the millimeters range, the propagating Lamb-wave modes can interact with discontinuities in these dimensions as well. Typical macroscopic damage modes found in the millimeters range are inter-ply delamination, inter-fiber cracks or fiber breakage crossing one or multiple plies. Such damage is often encountered in carbon fiber-reinforced plastics as a consequence of impact damage, proof testing of vessel structures or as manufacturing error. The current study presents results of finite element calculations to investigate the influence of those discontinuities on the propagation behavior of distinct Lamb-wave modes.

## 1. Introduction

Among the class of engineering materials, fiber-reinforced plastics show extraordinary high strength-to-weight and stiffness-to-weight ratios. This makes them ideal materials for construction of aircraft, high-performance cars or sporting goods. The design of fiber-reinforced structures relies on the anisotropy of the elastic properties caused by the alignment of carbon fibers. While this anisotropy is advantageous for constructional aspects, it causes major challenges for non-destructive evaluation (NDE) of these structures. Such NDE monitoring of the structural integrity is often done by acoustic emission (AE) analysis or active guided wave monitoring. Both methods rely on the propagation of acoustic waves in flat, plate-like structures. Plate waves are the dominant mode of wave propagation in those structures, and these waves are also known as Lamb waves [Lamb, 1917]. The infinite number of Lamb wave modes, which can exist within a plate is of two types. One type shows symmetric and the other shows anti-symmetric motion with respect to the mid-plane of the plate. However, the types of modes found most often in thin-walled fiber-reinforced structures are the fundamental symmetric mode ( $S_0$ ) and anti-symmetric mode ( $A_0$ ), often referred to as extensional and flexural mode. Lamb-wave propagation in undamaged carbon fiber-reinforced polymers (CFRP) has been investigated extensively before [Lowe, 1995, Castaings, 2004, Wang, 2007, Sause, 2010d]. Scattering of Lamb waves at internal damage, like cracks or delamination, is the key principle for structural health monitoring (SHM) of CFRP by guided wave testing [Raghavan, 2007]. The impact of such discontinuities on AE analysis has been investigated less. Since Lamb-wave propagation is the carrier of information on AE source activity in the material, distortion of information due to interaction of Lamb waves with internal discontinuities is closely related to the question of reliability of the information.

Changes of modal intensity or occurrence of alternative propagation paths due to scattering can readily affect source localization accuracy and/or complicate source identification procedures. This was recently demonstrated for the case of metallic obstacles, as encountered as fasteners in composite structures [Sause, 2012d]. The purpose of the current study is the extension of the previous investigation to internal discontinuities as typically faced for the case of damaged composite structures. Using finite element modeling (FEM), the interaction of Lamb waves with discontinuities is easy to visualize. It was recently demonstrated that this approach yields results consistent with experiments [Sause, 2010d, Sause, 2012b, Sause, 2012c, Sause, 2012d].

## 2. Finite Element Modeling

In the following, a finite element modeling approach is applied using the software program “ComsolMultiphysics”. All descriptions only refer to the way of implementation within the module “Structural Mechanics” of this software.

### 2a. Simulation methodology

The calculation of stress-strain relationships is based on the structural mechanics constitutive equation. Based on the principle of virtual work the program solves the partial differential equations for equilibrium conditions, expressed in global or local stress and strain components for an external stimulation.

For linear elastic media with elastic coefficients  $\vec{D}$ , Hooks law is chosen as the constitutive equation.

$$\vec{\sigma} = \vec{D} \cdot \vec{\varepsilon} \quad (1)$$

In the general case for anisotropic media the elasticity tensor  $\vec{D}$  is a 6 x 6 matrix with 12 independent components. Using the Voigt notation convention, the stress tensor can be written as vector  $\vec{\sigma}$  with six independent components composed of normal stresses  $\sigma$  and shear stresses  $\tau$ . The strain tensor is written similarly as vector  $\vec{\varepsilon}$ , which also has six independent components consisting of normal components  $\varepsilon$  and shear strain components  $\gamma$ . In the case of isotropic media the elasticity tensor is completely described by Young’s modulus  $E$  and the Poisson ratio  $\nu$ .

The principle of virtual work states that the variation of  $W$  induced by forces  $F_i$  and virtual displacements  $du_i$  in an equilibrium state equals zero:

$$\delta W = \sum_i F_i \cdot \delta u_i = 0 \quad (2)$$

Generally, the external applied virtual work equals the internal virtual work and in the case of a deformable body with volume  $V$  and surface  $S$ , results in a deformation state with new internal stress and strain components.

$$\int_S \delta \vec{u}^t \cdot \vec{F}_S dS + \int_V \delta \vec{u}^t \cdot \vec{F}_V dV - \int_V \delta \vec{\varepsilon}^t \cdot \vec{\sigma} dV = 0 \quad (3)$$

The external applied forces  $\vec{F}_S$  and  $\vec{F}_V$  act on the surface and volume of the body, respectively. The constraint forces within the material are expressed by consistent internal stress  $\vec{\sigma}$  and strain  $\vec{\varepsilon}$  components, with the superscript  $t$  indicating the transposed vectors.

To extend the principle of virtual work for dynamic systems, mass accelerations are introduced. This yields the formulation of the d'Alembert principle, which states that a state of dynamic equilibrium exists if the virtual work for arbitrary virtual displacements vanishes. Taking this into account and introducing the material density  $\rho$ , equation (3) becomes:

$$\int_S \delta \vec{u}^t \cdot \vec{F}_S dS + \int_V \delta \vec{u}^t \cdot \vec{F}_V dV - \int_V \delta \vec{\epsilon}^t \cdot \vec{\sigma} dV - \int_V \rho \frac{\partial^2 \vec{u}}{\partial t^2} \cdot \delta \vec{u} dV = 0 \quad (4)$$

This defines the basic differential equation solved for every finite element. In order to model structural mechanics problems, a suitable geometry and respective boundary conditions have to be defined.

## 2b. Model description

The model setup used in this study is shown in Fig. 1. A rectangular plate of 400 mm  $\times$  400 mm size and 1 mm thickness is used as propagation medium. Elastic properties of unidirectional CFRP plate are used as given in Table 1. Fiber direction of the unidirectional lamina is oriented along the 0° axis as noted in Fig. 1. Two symmetry planes were chosen to reduce the volume modeled to one quarter of the overall volume. The symmetry planes are the yz- and xz-plane with respect to the origin of the coordinate system.

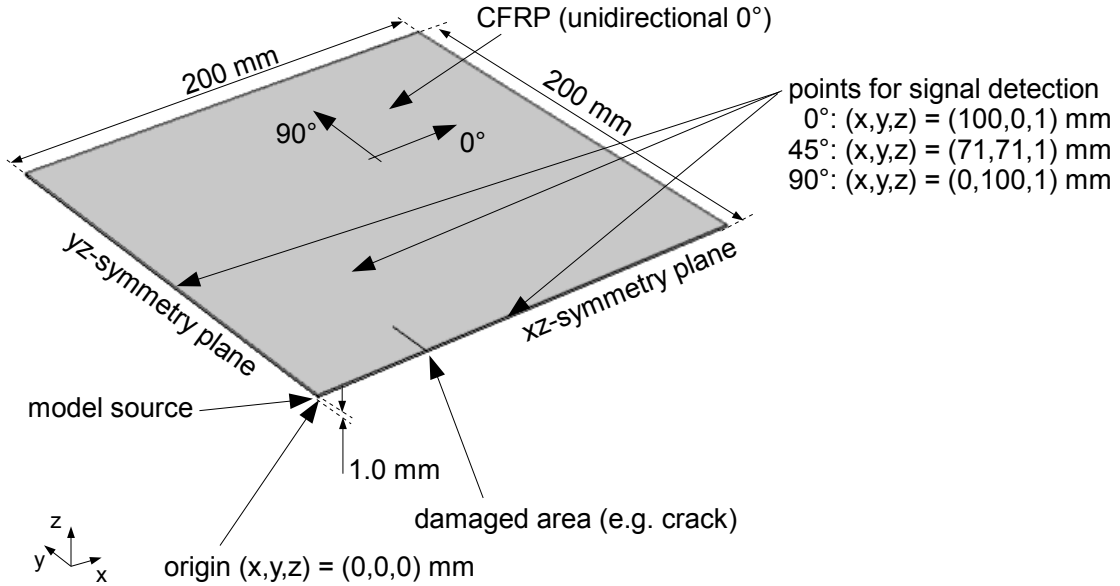


Fig. 1. 3-dimensional model setup used for simulation of Lamb-wave propagation.

As AE source model, a point dipole was chosen following [Gary, 1994]. As demonstrated in [Hamstad, 2002] such point dipoles can be used to excite particular fundamental Lamb-wave modes in isotropic plates. In contrast to complex source models based on micromechanical considerations [Sause, 2010a, Sause, 2010b], point dipoles are computationally more efficient to investigate Lamb-wave propagation in larger structures. The position of the point dipole was chosen at (x, y, z) = (0.00, 0.00, 0.53) mm, slightly asymmetric with respect to the mid-plane of the plate, to excite a reasonable amount of  $S_0$  and  $A_0$  Lamb wave modes at the same time. The length of the dipole (oriented in x-direction) was chosen to be 200  $\mu$ m. A linear ramp function with excitation time  $t_e = 1 \mu$ s and maximum force  $F_{\max} = 3$  N was used.

$$F(t) = \begin{cases} F_{\max} \cdot (t/t_e) & t \leq t_e \\ F_{\max} & t > t_e \end{cases} \quad (5)$$

All signals are evaluated at 100-mm distance to the AE source in 0°, 45° and 90° propagation direction as z-displacement on the top surface of the plate.

The region of internal damage starts at a distance of 50 mm from the source in the 0°-direction. This configuration was chosen, since complementary studies with obstacles placed in 90° orientation to the fibers confirmed that the influence of the obstacles is largest in the 0° case. Details of the various configurations are shown in Figs. 2-4. Each of the modeled geometries refers to one prototype of internal damage.

Inter-fiber cracks (also called matrix cracks) weaken the link between neighboring fibers and can thus affect the transmission of acoustic waves. In the chosen configuration, the growth direction of such cracks is along the fiber axis direction (0°). From the perspective of wave propagation, the worst case is a growth of such cracks through the complete thickness. This configuration is studied here as cut through the plate with width of 25  $\mu\text{m}$  and various lengths as shown in Fig. 2.

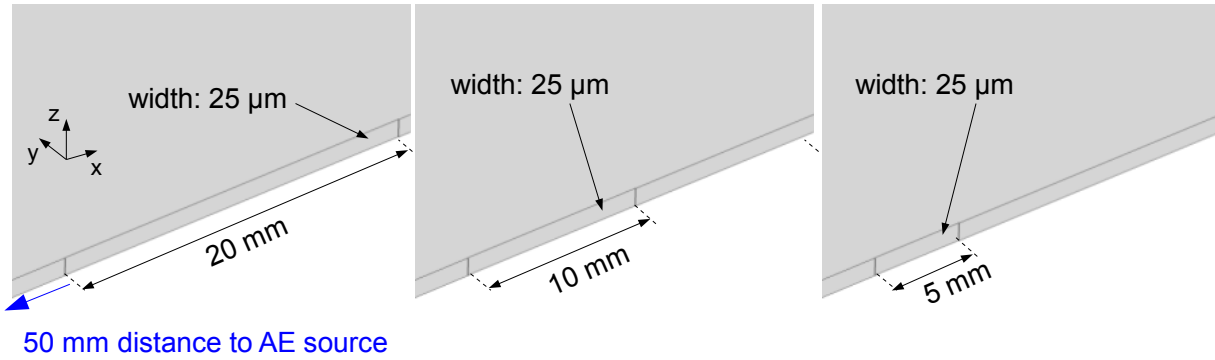


Fig. 2. 3-dimensional model geometry used for simulation of inter-fiber cracks (cut along fiber axis direction).

As the second prototype, rupture of fibers can accumulate locally and can become a macroscopic crack. In the current configuration this is modeled as a 100- $\mu\text{m}$  thick cut perpendicular to the fiber axis direction as shown in Fig. 3. Since such crack growth typically initiates ultimate failure of the load carrying structure, we investigated three depths of the cut to investigate the influence on wave propagation. The depth of 0.5 mm already refers to a significant amount of damage, reflecting a rupture of more than 800,000 fiber filaments. Also, for bending loads, the initiation of these cracks is typically found on the surface of the structure. Therefore, the current model, with damage starting on the surface, exhibits an asymmetric location of the crack with respect to the mid-plane.

The third prototype is inter-ply delamination. This is an in-plane discontinuity that weakens the local bending stiffness of the plate and is often encountered in fiber-reinforced structures as a consequence of impact damage, excessive loading or even as residue of the manufacturing process. Since this can occur in various extents, we investigate three different sizes to reflect reasonable variability of the size of the delaminated area. For all configurations a thickness of the delamination of 50  $\mu\text{m}$  is chosen, centered within the plate.

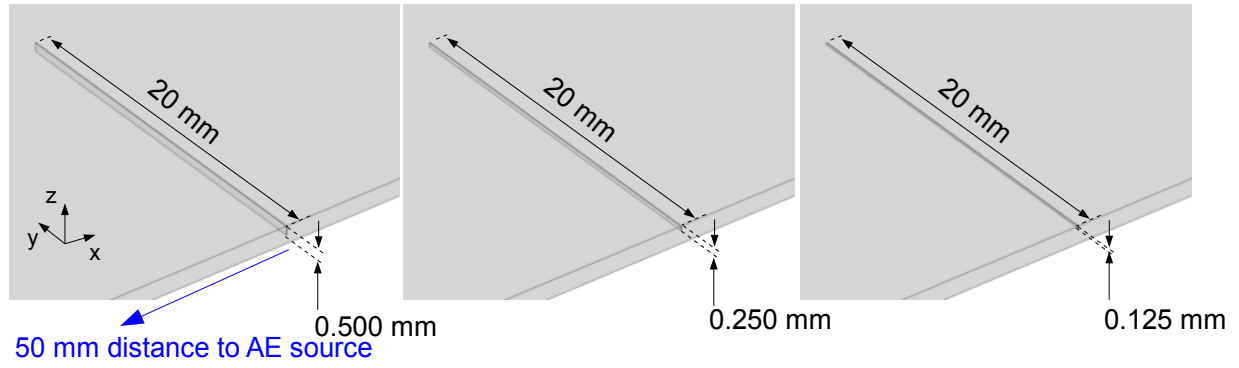


Fig. 3. 3-dimensional model geometry used for simulation of broken fibers (cut perpendicular to fiber axis direction).

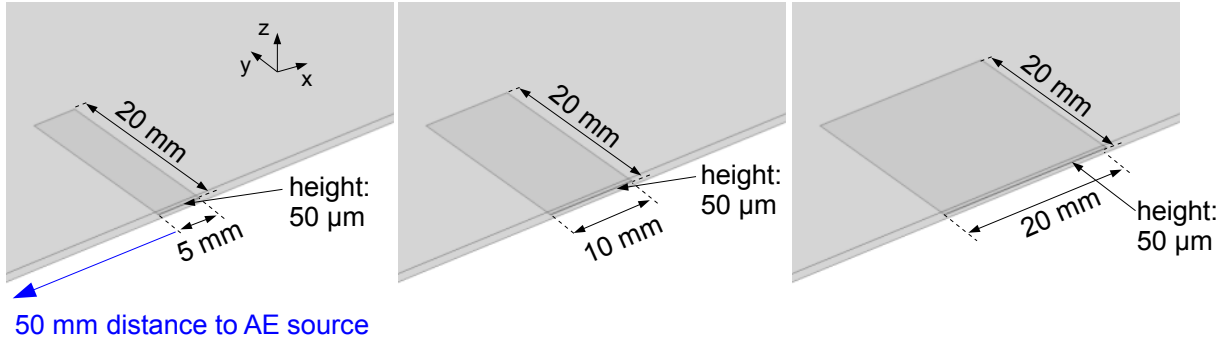


Fig. 4. 3-dimensional model geometry used for simulation of inter-ply delamination (cut parallel to fiber axis direction).

Table 1. List of elastic properties used for finite element modeling.

	Density [kg/m <sup>3</sup> ]	Elasticity Constants [GPa]
T800/913 (unidirectional)	1550	$C_{11}=154.0$ $C_{12}=C_{13}=3.7$ $C_{22}=C_{33}=9.5$ $C_{23}=5.2$ $C_{44}=2.5$ $C_{66}=C_{55}=4.2$

For accurate resolution of calculated signals, a maximum element size of 1.0 mm edge length was chosen for tetrahedral mesh elements with quadratic order of the geometry shape functions. To resolve geometric details in narrow regions the mesh was locally refined down to a minimum edge length of 5  $\mu\text{m}$ . The temporal resolution was chosen to be 100 ns and results were calculated for the first 100  $\mu\text{s}$  after signal excitation. Convergence of simulation results with respect to mesh resolution and temporal resolution was previously checked by subsequent refinement. To this end mesh resolution was increased to 0.5 mm edge length and temporal resolution was increased to 5 ns. Results of these calculations were found to have a coherence level  $\geq 0.998$  to the current settings within the frequency range between 1 kHz and 2 MHz.

#### 4. Results

In the following, the influence of the modeled damage on the signal propagation is investigated. Figure 5 shows the Choi-Williams distribution (CWD) of the calculation result for signal

propagation along the  $0^\circ$  axis of the unidirectional CFRP plate [Choi, 1989]. The CWD in Fig. 5-a uses a different color, frequency and time range than Fig. 5-b, which is used to emphasize the  $S_0$ -mode at the initial part of the signal. To identify particular Lamb wave modes, the dispersion curves of the fundamental modes were calculated by the software package provided by [Zeyede, 2010]. As indicated by the superimposed dispersion curves for the  $S_0$ -mode at 100 mm and 300 mm source distance, the  $S_0$ -mode is reflected at the edge of the plate in x-direction and is detected more than once. The CWD result of the  $A_0$ -mode shown in Fig. 3-b agrees well with the calculated result of the  $A_0$  dispersion curve for 100 mm distance. The small dips in the curve seen at  $52 \mu\text{s}$  and  $62 \mu\text{s}$  are caused by multiple reflections of the  $S_0$ -mode, which has been re-reflected at all edges of the plate at this time. The calculation results for the pure CFRP plate in Fig. 5 will act as a reference case to evaluate the influence of any damage modeled within the propagation path. A comparison of the calculated wave-fields will be made in section 5.

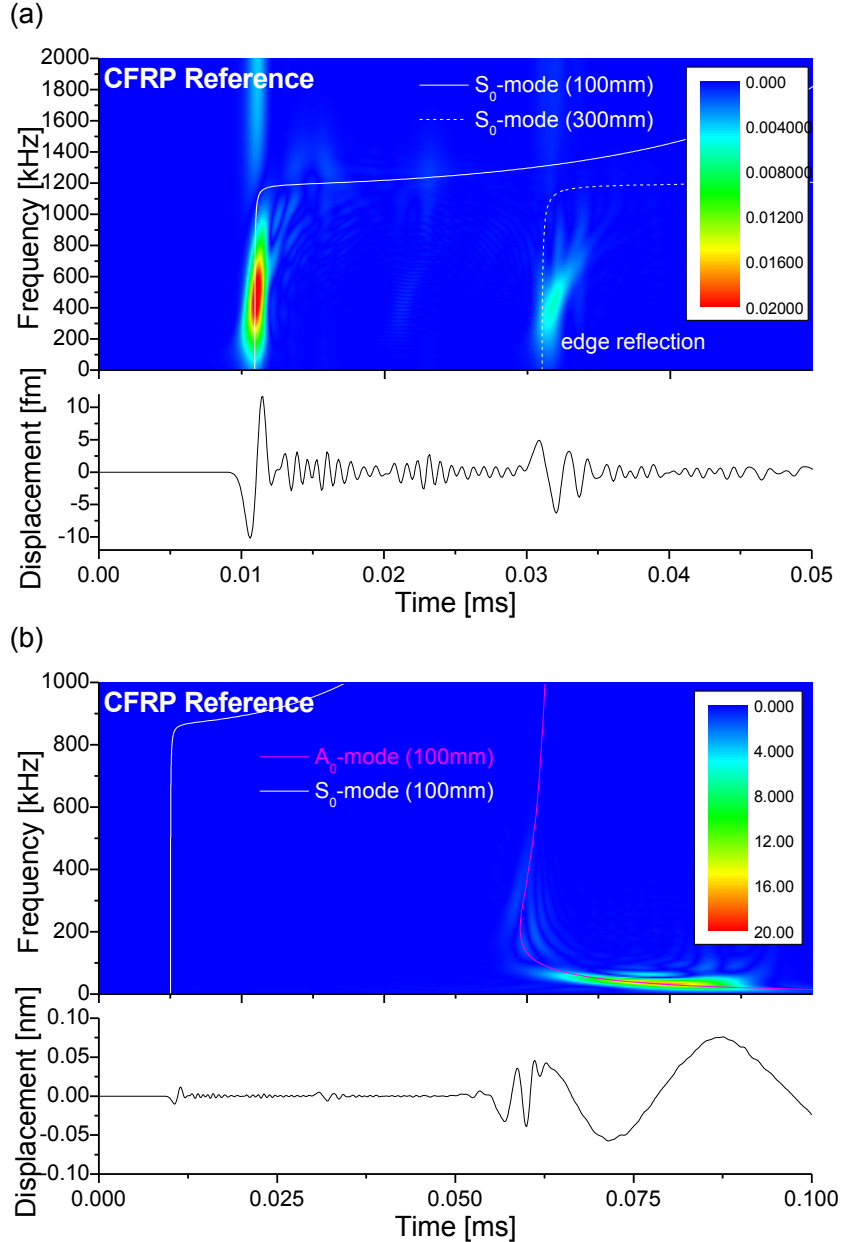


Fig. 5. Simulation results of signal propagation at 100 mm distance along  $0^\circ$  direction in unidirectional CFRP. Truncated time scale shows  $S_0$ -mode (a) and full time scale shows  $A_0$ -mode (b).

#### 4a. Inter-fiber cracks

Inter-fiber cracks are one of the basic damage types found in fiber-reinforced composites. These are cracks with propagation direction parallel to the fiber axis direction. Since the strength of the direction perpendicular to the fiber axis is the weak link between the fibers, this type of damage is observed frequently in composite structures. In the current configuration, the inter-fiber crack is modeled as crack-through process, i.e. the crack reaches from the top to the bottom of the plate. The length of the inter-fiber crack is varied between 5 mm and 20 mm to cover a broad range of macroscopic crack sizes.

As seen in Fig. 6 for the  $S_0$ -mode detected in damaged structures, there are only negligible differences compared to the reference case. In contrast, there is a detectable influence of the presence of the inter-fiber cracks on the initial part of the  $A_0$ -mode. For the various lengths of 5 mm, 10 mm and 20 mm of the inter-fiber crack no significant differences are observed relative to each other besides a small signature at 63  $\mu$ s.

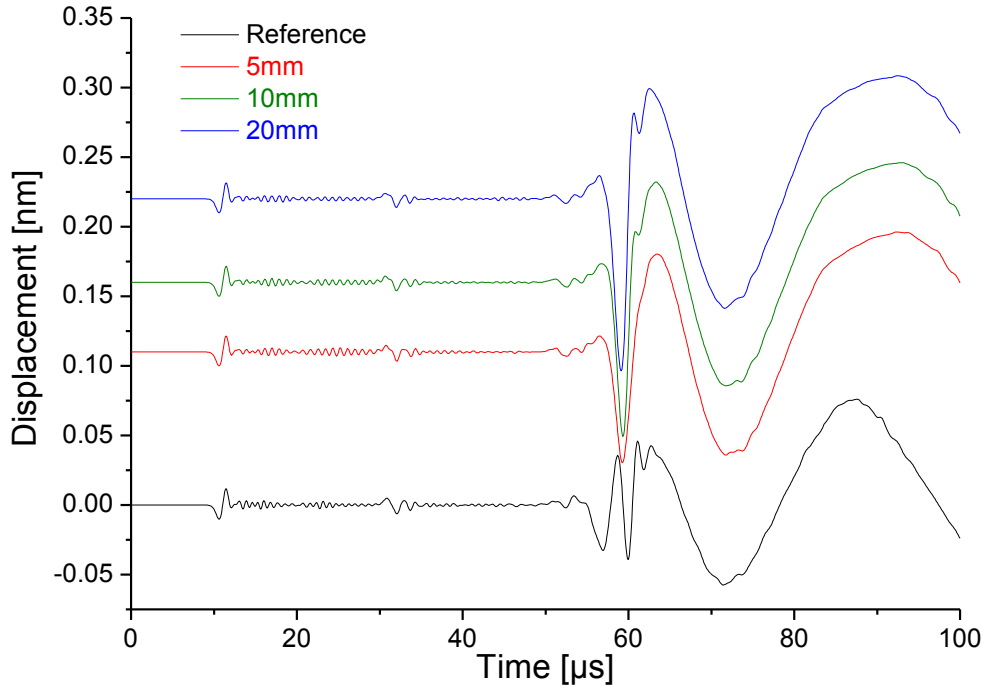


Fig. 6. Simulation results of signal after propagation of 100 mm along  $0^\circ$  direction in unidirectional CFRP with inter-fiber cracks of various lengths.

#### 4b. Broken fibers

Among the damage types found in fiber-reinforced composites, a rupture of the load bearing constituents is the most severe damage. In the current model, the presence of such discontinuous fiber filaments is taken into account by an air gap with extension perpendicular to the fiber axis direction (see Fig. 3). To take into account the various degrees of damage for this type of failure, the depth of the air gap in the plate thickness direction is varied between 0.125 mm and 0.500 mm.

As seen in Fig. 7, the influence of the discontinuity on the first arrival of the  $S_0$ -mode ( $t < 20 \mu$ s) is negligible for all cases investigated. Dependent on the through-thickness dimension of the modeled discontinuity, a secondary peak arises around 35  $\mu$ s. This is caused by modal conversion of the incident primary  $S_0$ -mode at the discontinuity into a secondary  $A_0$ -mode and

into a secondary  $S_0$ -mode (see Fig. 9 and Fig. 10, also [Sause, 2012d]). The later parts of the signal ( $t > 40 \mu s$ ) are also affected by this interaction, which causes a superposition of the incident  $A_0$ -mode with the multiple reflections of the secondary modes. It is worth noting that the model is energy conservative. Still, the calculated amplitude of the signals is distinctly different. This is solely caused by the presence of the broken fibers, which cause a preferential scattering of the displacement field, which transfers energy from the in-plane displacement to the out-of-plane displacement.

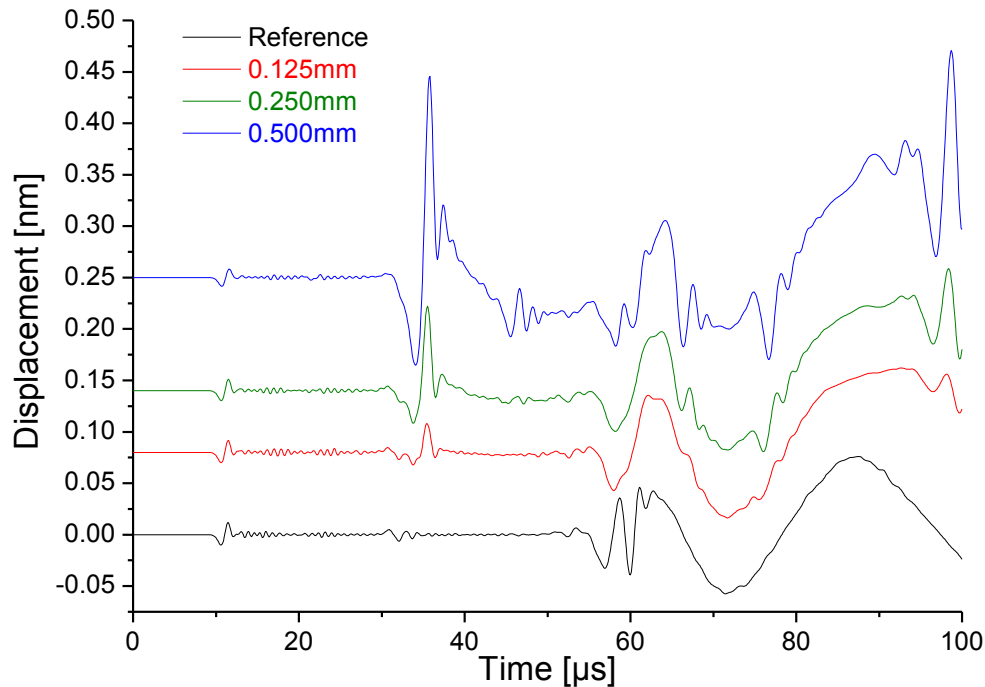


Fig. 7. Simulation results of signal after propagation of 100 mm along  $0^\circ$  direction in unidirectional CFRP with broken fibers modeled with various dimensions.

#### 4c Inter-ply delamination

Inter-ply delamination is one of the most common types of damage found in fiber-reinforced composites, since it is often caused by local impact or as residue of a manufacturing error. During mechanical testing of fiber-reinforced structures, delamination can evolve step by step and can affect the elastic properties along the signal propagation path. Thus, the influence of delamination on the detected AE signals is of considerable interest. To resemble the variety of dimensions of inter-ply delamination, the size of the delaminated area in the in-plane direction was varied between 5 mm and 20 mm (see Fig. 4).

Figure 8 shows the calculated signals for all three inter-ply delamination sizes investigated and the reference signal for comparison. For the  $S_0$ -mode there are only negligible differences observed to the reference case. Since propagation of the  $S_0$ -mode is dominated by the in-plane stiffness, this is explained by considering a multi-layer specimen composed of  $950 \mu m$  CFRP and  $50 \mu m$  air. The in-plane stiffness of such a plate is as close as 95 % of the stiffness of a pure  $1000\text{-}\mu m$  CFRP plate. A larger influence is observed for the propagation behavior of the  $A_0$ -mode. The shape and intensity of the  $A_0$ -modes differ from the reference signal due to the change of local bending stiffness as introduced by the inter-ply delamination. With increasing size of the inter-ply delamination, the deviation compared to the reference case increases as well.



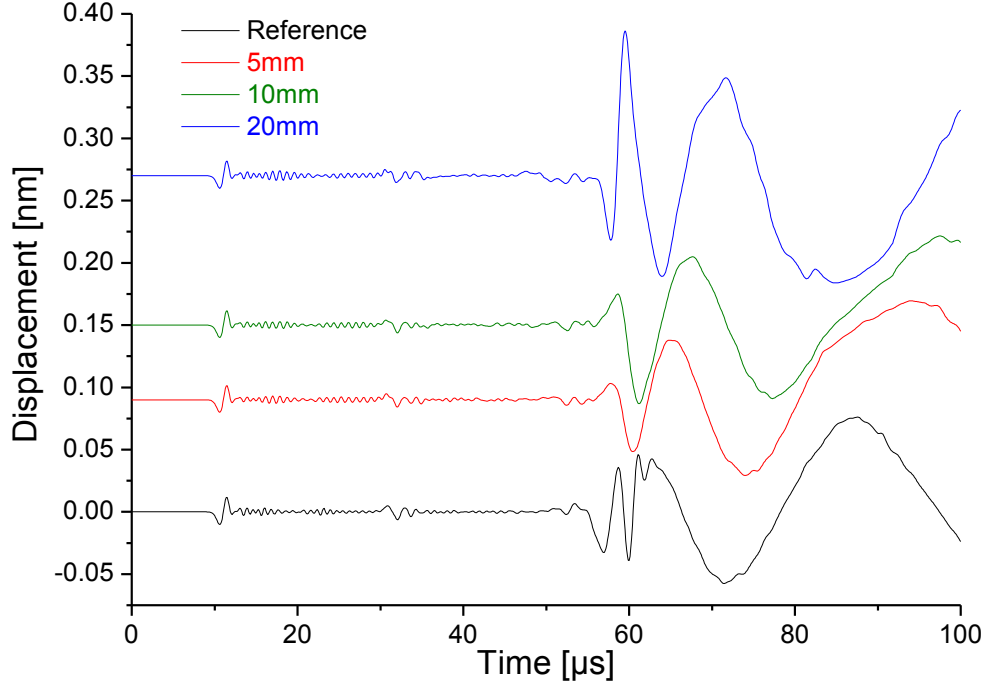


Fig. 8. Simulation results of signal after propagation of 100 mm along  $0^\circ$  direction in unidirectional CFRP with inter-ply delamination of various dimensions.

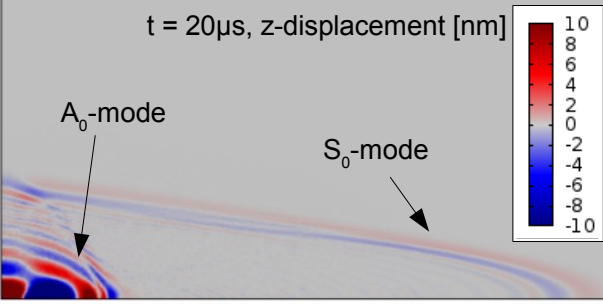
## 5. Discussion

In the present study, the interaction of Lamb-wave modes with different types of internal damage in unidirectional CFRP plates was investigated by means of finite element modeling. For evaluation of the signals a unidirectional CFRP plate was chosen as propagation medium, since this exhibits a maximal elastic anisotropy. The wave fields obtained for the reference case without obstacles, a modeled 20-mm long inter-fiber crack, a 0.5-mm deep broken fibers and a 10-mm long inter-ply delamination are shown in Figs. 9 and 10 for two distinct times  $t = 20 \mu s$  and  $t = 40 \mu s$  after signal excitation.

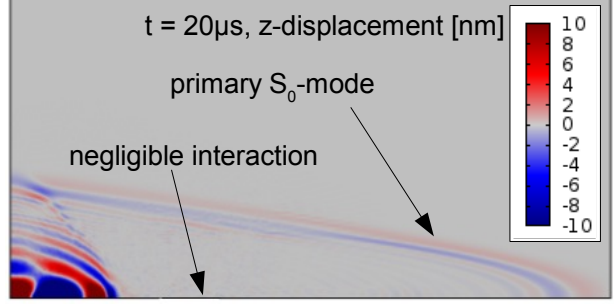
The interaction of the different types of damage with the incident  $S_0$ -mode is visualized best in the wave-fields in Fig. 9. For the inter-fiber cracks and inter-ply delamination, only weak interaction with the  $S_0$ -mode is found. In contrast, for the broken fibers, the incident  $S_0$ -mode causes excitation of a strong secondary  $A_0$ -mode with a radiation pattern around the crack, which acts as an epicenter. This is caused by a modal conversion of the primary  $S_0$ -mode into a secondary  $A_0$ -mode, since the primary wave front of the  $A_0$ -mode did not arrive at the position of the modeled crack for  $t < 20 \mu s$ . Subsequent to the emission of the secondary  $A_0$ -mode, an excitation of a secondary  $S_0$ -mode is observed as well.

In Fig. 10, the wave field for  $t = 40 \mu s$  shows the interaction of the  $A_0$ -mode with the different types of modeled damage. Again only weak interaction is found between the  $A_0$ -mode and the modeled inter-fiber cracks or the modeled inter-ply delamination as shown in Figs. 10-b and 10-c. For the broken fibers, similar as for the incident  $S_0$ -mode, the  $A_0$ -mode is significantly affected by the presence of the discontinuity.

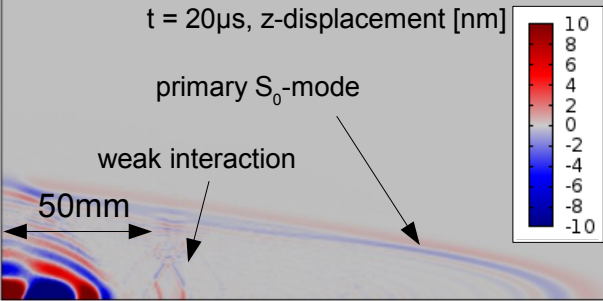
a) Reference (pure CFRP)



b) Inter-Fiber cracks



c) Delamination



d) Broken Fibers

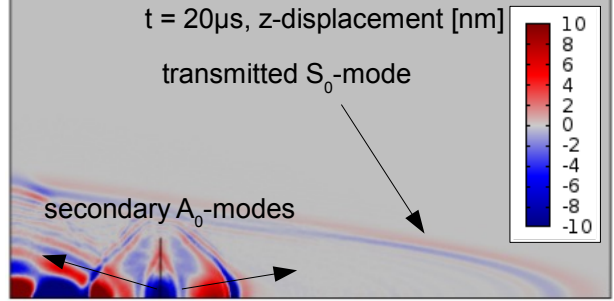
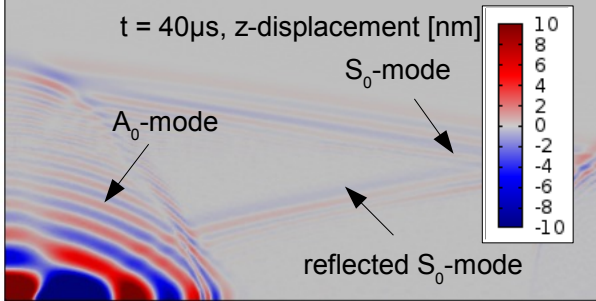
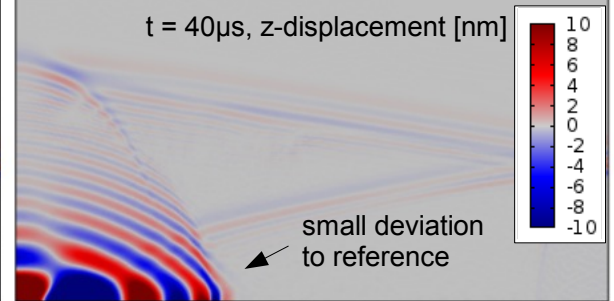


Fig. 9. Comparison of simulated wave fields of z-displacement for reference (a), 10-mm inter-fiber crack (b), 10-mm delamination (c) and 0.5-mm broken fibers (d) at  $t = 20\mu\text{s}$  after signal excitation.

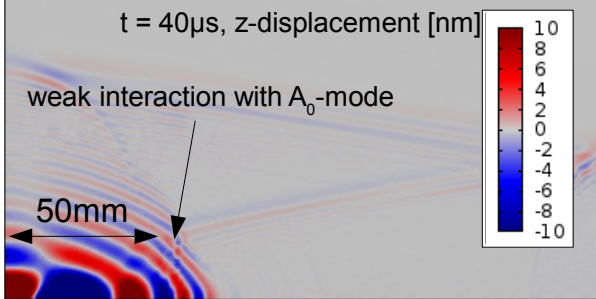
a) Reference (pure CFRP)



b) Inter-Fiber cracks



c) Delamination



d) Broken Fibers

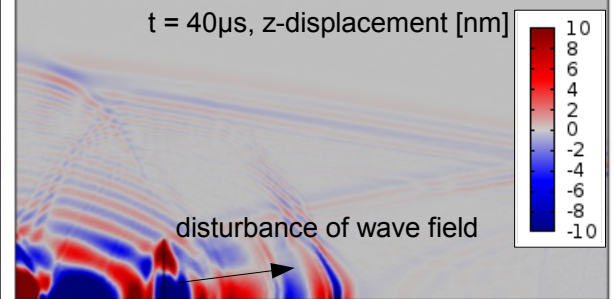


Fig. 10. Comparison of simulated wave fields z-displacement for reference (a), 10 mm inter-fiber crack (b), 10 mm delamination (c) and 0.5 mm broken fibers (d) at  $t = 40\mu\text{s}$  after signal excitation.

In order to investigate the influence of the simulated damage on AE analysis, the calculated signals are processed in a similar way as typical for experimental signals. Thus, AE features are extracted from the signals and arrival times of the  $S_0$ -mode and the  $A_0$ -mode are calculated for a distance of 100 mm in all propagation directions of  $0^\circ$ ,  $45^\circ$  and  $90^\circ$ . Table 2 lists all AE parameters and arrival times of the cases studied. For calculation of signal energies and signal amplitude an artificial sensor sensitivity of  $4.5 \times 10^9$  V/m was assumed.

Table 2. Definition of AE features.

AE feature	Definition
Amplitude [mV]	$U_{max}$
Absolute energy [J]	$E = \int_0^{t_{AE}} U(t)^2 / 10k \square dt$
Peak frequency [kHz]	$f_{peak}$
Frequency centroid [kHz]	$f_{centroid} = \frac{\int f \cdot \tilde{U}(f) df}{\int \tilde{U}(f) df}$
Weighted Peak frequency [kHz]	$f_{wpeak} = \sqrt{f_{peak} \cdot f_{centroid}}$
Partial Power 1 [%]	$\frac{\int_{f_1}^{f_2} \tilde{U}^2(f) df}{\int_{0kHz}^{1200kHz} \tilde{U}^2(f) df}$
Partial Power 2 [%]	
Partial Power 3 [%]	PP1: $f_1 = 0$ kHz; $f_2 = 150$ kHz
Partial Power 4 [%]	PP2: $f_1 = 150$ kHz; $f_2 = 300$ kHz
Partial Power 5 [%]	PP3: $f_1 = 300$ kHz; $f_2 = 450$ kHz
Partial Power 6 [%]	PP4: $f_1 = 450$ kHz; $f_2 = 600$ kHz
	PP5: $f_1 = 600$ kHz; $f_2 = 900$ kHz
	PP6: $f_1 = 900$ kHz; $f_2 = 1200$ kHz

$$\text{Partial Power} = \frac{\int_{f_1}^{f_2} \tilde{U}^2(f) df}{\int_{0kHz}^{1200kHz} \tilde{U}^2(f) df}$$

The definition of features is based on the basic properties derived from the signal in time domain  $U(t)$  and in frequency domain  $\tilde{U}(f)$  as shown in Figs. 11-a and 11-b, respectively.  $U_{max}$  is the maximum signal amplitude, as seen in Fig. 11-a, while the absolute energy is derived from the integral of  $U(t)^2$  within the investigated time of 100  $\mu$ s.  $f_{peak}$  defines the frequency position of maximum FFT-magnitude as seen in Fig. 11-b, while  $f_{centroid}$  is defined in Table 2. Definition of the different Partial Power features is given in Table 2 as well.

Arrival times of  $S_0$ -mode and  $A_0$ -mode are picked from the CWDs following the method introduced by Hamstad et al. [Hamstad, 2008]. Thus, arrival of the mode is picked as the time of maximum coefficient intensity of the respective mode at a constant frequency (500 kHz in the current case).

In the following, the influence of the internal damage types on the extracted signal features is discussed using the initial arrival time ( $S_0$ -mode arrival), the signal amplitude and the weighted peak frequency representative for the other features of Table 3.

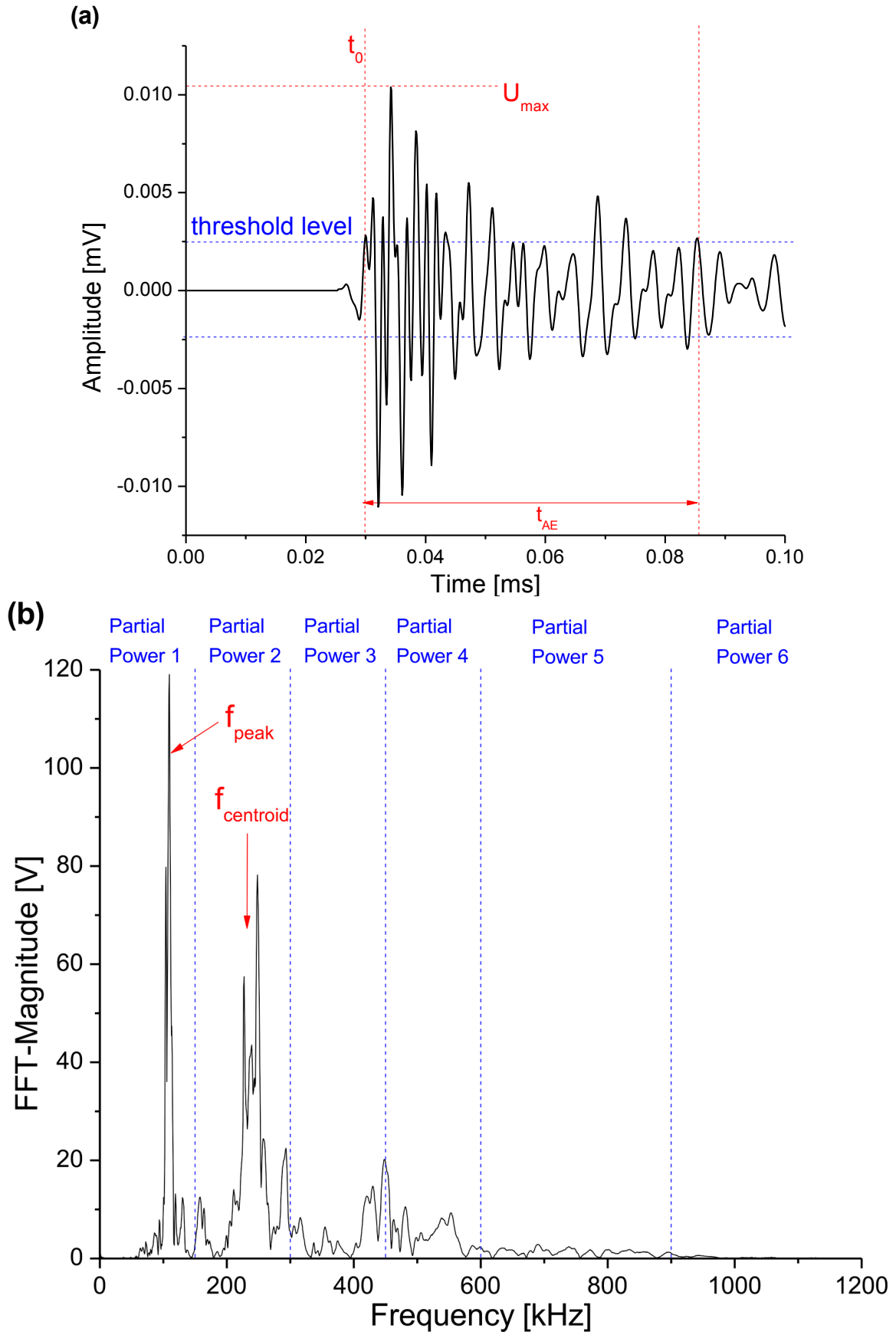


Fig. 11. Extraction of features from acoustic emission signals in time (a) and frequency domain (b).

Table 3. Values of AE features extracted from the calculated signals in various propagation directions.

	Configuration	Arrival time $S_0$ [ $\mu$ s]	Arrival time $A_0$ [ $\mu$ s]	Amplitude [mV]	Absolute energy [nJ]	Peak frequency [kHz]	Weighted Peak frequency [kHz]	Frequency centroid [kHz]	Partial Power 1 [%]	Partial Power 2 [%]	Partial Power 3 [%]	Partial Power 4 [%]	Partial Power 5 [%]	Partial Power 6 [%]
Reference														
0°	1	9.2	81.6	342.5	23.4	39.1	124.5	396.5	59.5	13.3	13.7	7.0	10.9	1.6
45°	11	23.8	90.2	30.5	23.6	127.0	232.4	425.3	38.6	21.2	17.8	9.2	23.4	2.3
90°	21	33.5	44.6	24.9	23.6	293.0	504.9	870.0	16.0	18.4	17.9	8.9	2.2	15.5
Inter-fiber cracks														
5mm-0°	2	9.3	91.7	388.2	55.6	29.3	72.3	178.4	77.6	12.8	4.3	1.7	11.8	1.5
5mm-45°	12	24.8	90.2	32.3	55.8	87.9	229.9	601.4	30.6	15.3	23.1	17.0	15.6	2.2
5mm-90°	22	35.6	37.0	26.5	55.8	117.2	234.2	468.2	20.9	23.6	24.1	14.3	2.3	1.5
10mm-0°	3	9.2	91.8	498.3	58.0	29.3	73.7	185.5	68.7	15.4	8.7	3.8	8.0	1.1
10mm-45°	13	24.7	90.2	31.4	58.2	87.9	223.7	569.3	40.6	21.6	18.0	9.4	13.6	2.4
10mm-90°	23	31.9	40.8	24.2	58.3	263.7	353.6	474.2	22.0	24.4	25.1	13.7	2.1	1.2
20mm-0°	4	8.9	91.5	556.4	64.1	29.3	71.7	175.7	66.3	17.0	9.6	4.2	8.5	0.9
20mm-45°	14	23.1	90.2	32.0	64.4	87.9	225.6	579.2	41.5	20.8	17.6	9.2	18.5	2.5
20mm-90°	24	29.3	40.6	30.4	64.4	263.7	338.7	435.0	19.9	23.0	24.4	13.3	3.6	0.9
Fiber breaks														
0.125mm-0°	5	9.4	90.0	369.7	44.1	29.3	70.2	168.1	77.9	7.7	5.9	3.6	11.9	1.3
0.125mm-45°	15	25.6	90.2	29.8	44.3	87.9	229.1	597.3	42.2	16.9	18.1	8.4	19.0	2.5
0.125mm-90°	25	31.8	37.0	30.0	44.3	439.5	438.8	438.2	16.7	20.6	27.5	15.4	4.9	0.8
0.25mm-0°	6	9.4	90.0	533.7	54.0	19.5	64.8	214.9	63.0	13.3	11.1	6.8	16.5	0.9
0.25mm-45°	16	25.3	92.5	37.5	54.2	87.9	227.2	587.6	36.6	15.0	18.1	11.7	19.0	2.2
0.25mm-90°	26	31.7	36.9	29.7	54.3	439.5	423.6	408.3	17.0	20.0	25.0	17.0	6.0	1.0
0.5mm-0°	7	9.4	90.8	993.1	122.0	9.8	60.3	372.9	50.0	19.0	15.0	9.0	10.6	1.0
0.5mm-45°	17	23.7	92.5	45.3	122.0	87.9	220.5	553.1	37.3	15.1	22.9	12.3	21.0	1.9
0.5mm-90°	27	30.9	41.0	32.8	122.0	439.5	451.6	464.0	15.0	18.0	24.0	21.0	3.0	1.0
Delamination														
5mm-0°	8	9.4	92.3	358.0	39.5	29.3	85.7	250.8	81.0	9.0	3.0	2.0	10.0	2.0
5mm-45°	18	24.6	92.5	34.1	39.7	97.7	249.3	636.7	40.9	19.0	17.1	10.2	27.0	2.9
5mm-90°	28	29.7	36.8	31.4	39.8	293.0	368.1	462.6	14.0	18.0	22.0	17.0	4.0	1.0
10mm-0°	9	9.4	102.0	322.1	35.4	39.1	128.3	421.6	76.0	11.0	4.0	3.0	19.9	3.0
10mm-45°	19	24.8	39.2	35.1	35.7	97.7	247.3	626.4	36.0	20.0	12.7	9.0	29.0	2.3
10mm-90°	29	32.0	68.6	24.6	35.8	293.0	384.0	503.3	16.0	19.0	20.0	15.0	4.0	1.4
20mm-0°	10	9.4	42.0	523.6	59.0	39.1	146.8	552.0	62.0	18.0	9.0	4.0	7.5	3.0
20mm-45°	20	24.2	90.2	40.7	59.4	87.9	226.2	582.2	42.6	22.5	18.0	6.8	19.0	2.6
20mm-90°	30	29.3	71.0	31.1	59.5	175.8	281.1	449.5	21.0	23.0	21.0	14.0	10.9	2.0

### 5a. Influence on arrival time

In order to obtain valid source locations, a proper determination of the initial arrival time is a key requirement for most of the currently used localization algorithms. The significant influence of the various internal damage types on the propagation behavior of the signals was already demonstrated in section 4. In Fig. 12, the extracted initial arrival times are shown for all damage configurations and the reference case in 0°, 45° and 90° propagation direction. The largest influence of the internal damage types is found for the 90° propagation direction, which demonstrates, that the complete wave-field is affected by the presence of the damage and not solely the part of the wave propagating through the obstacle (0° direction).

Based on the maximum deviation of 4.2  $\mu\text{s}$  to the reference case of the calculated arrival time of the  $S_0$ -mode in 90° propagation direction, a corresponding error of localization in the range of several centimeters can be expected. The estimation is based on the calculated group velocity of the  $S_0$ -mode in 90° propagation direction.

A significantly larger influence was found for the arrival time of the  $A_0$  mode. Due to modal conversion occurring at the internal damage, the arrival of the first detectable  $A_0$ -mode is 48.6  $\mu\text{s}$  ahead compared to the reference case in one configuration. However, this is not the arrival of the primary  $A_0$  mode as discussed before. For the majority of the cases studied, the arrival times of the  $A_0$  mode are within 10  $\mu\text{s}$  difference to the reference case. Consequently, for localization methods using arrival times of both fundamental Lamb wave modes, the observed difference in arrival time of the  $A_0$  mode might have a large impact as well.

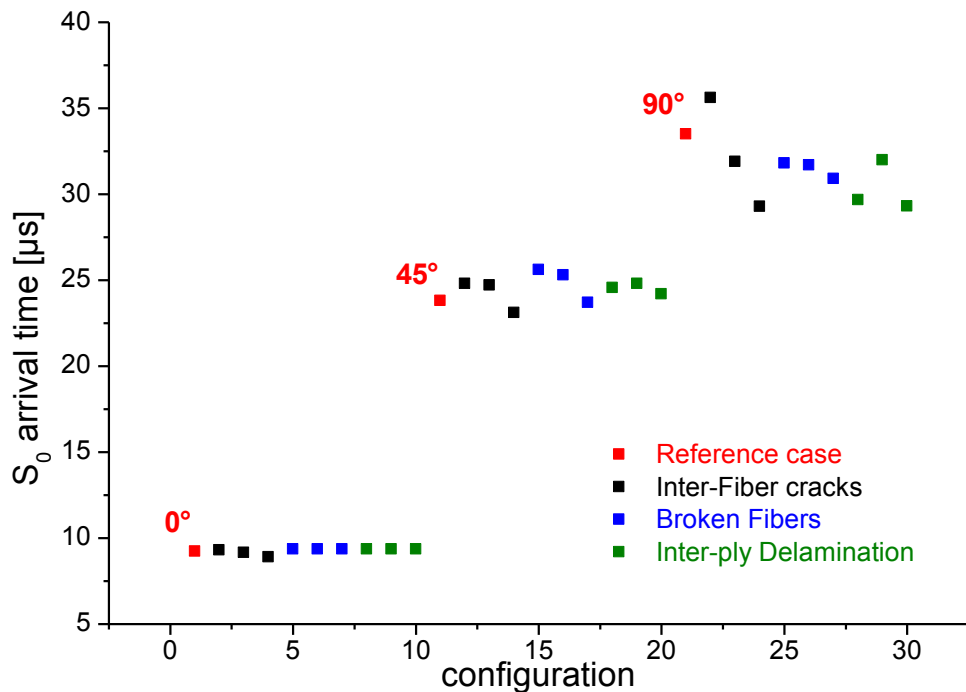


Fig. 12. Calculated arrival time of  $S_0$ -mode for the various configurations of internal damage in comparison to the reference case for 0°, 45° and 90° propagation direction.

### 5b. Influence on signal features

For source identification procedures one approach is the use of parameter-based pattern recognition [Sause, 2010c, Sause, 2010a, Sause, 2012a]. Since cracks and delamination are likely to evolve between AE source positions and the position of detection during specimen loading, their influence on the transmitted Lamb waves has to be understood thoroughly.

From the list of calculated features given in Table 2, some were found to deviate more than 100 % from the reference case. One example is the signal amplitude values shown in Fig. 13 for each configuration, evaluated in 0°, 45° and 90° propagation directions. Compared to the reference case (red), the signals passing through the damaged region experience large changes of their signal amplitude. This is due to the modal conversion at the damage position, and the scattering introduced by some of the damage types. These effects are not taken into account by the conventional definitions for calculation of signal amplitude or AE signal energies as given in Table 2. Except for configuration 7, the overall deviation of amplitude values was found to be within  $\pm 0.25$  V (i.e.  $\pm 5$  dB<sub>AE</sub>) to the reference case. Compared to the  $\pm 3$  dB<sub>AE</sub> recommendation of ASTM E 2191 for sensor replacement this amplitude range is well within typically encountered uncertainties of measurement setups used.

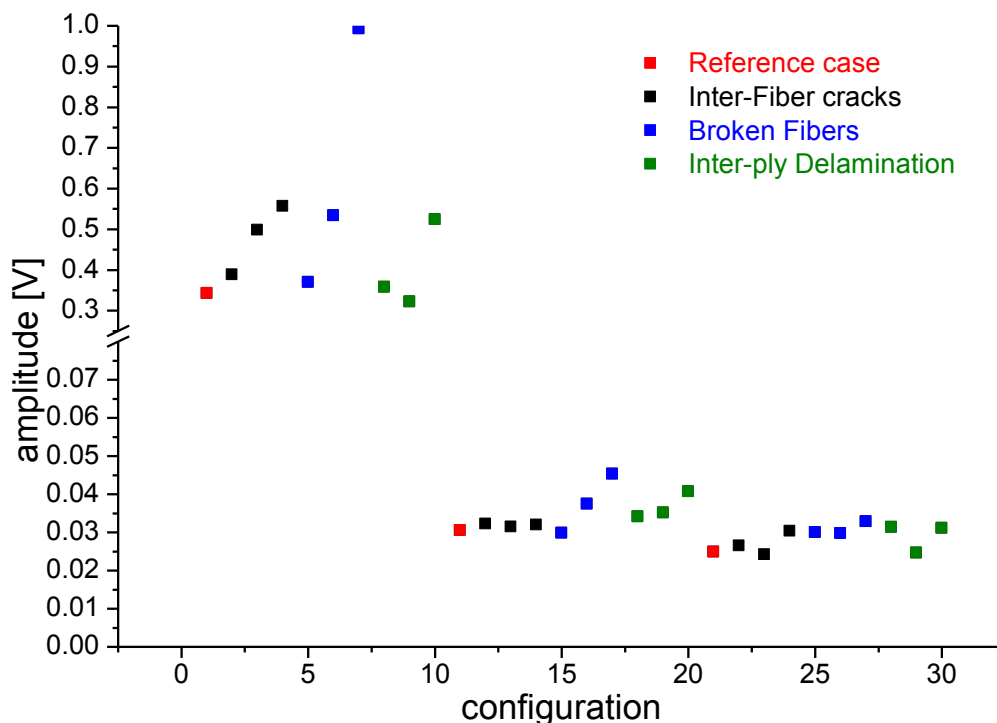


Fig. 13. Calculated signal amplitude of signals for the various configurations of internal damage in comparison to the reference case for 0°, 45° and 90° propagation direction.

The calculated weighted Peak-Frequency for the signals of different damage configurations and the reference case are shown in Fig. 14 for 0°, 45° and 90° propagation directions. Depend on the propagation angle, different values for the weighted peak frequency are observed. This is caused by the asymmetric propagation of Lamb-wave modes in the unidirectional plate modeled herein. Similar to the signal amplitude, deviations compared to the reference case are up to 100 %. Again, features evaluated in all propagation directions are affected by the presence of the modeled damage types. The range of feature values seems unacceptably high in order to perform

valid source identification based on frequency features, since the modeled source type is identical for all cases studied.

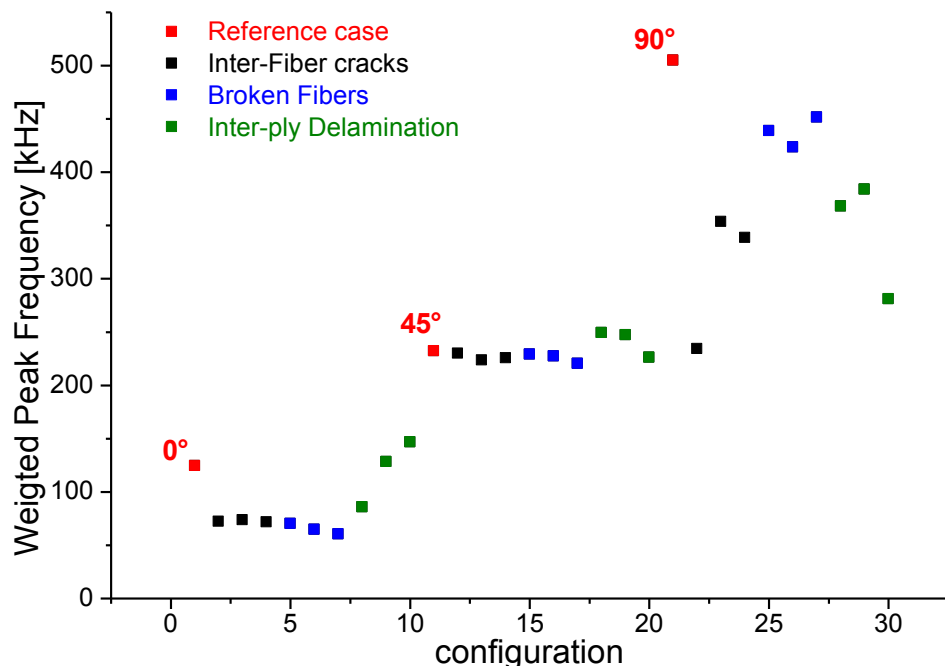


Fig. 14. Calculated weighted peak frequency of signals for the various configurations of internal damage in comparison to the reference case for 0°, 45° and 90° propagation direction.

However, for pattern recognition methods, there is a typical experimentally encountered distribution range for an individual feature. This is demonstrated in Fig. 15. Here, the experimentally detected signal features of a double cantilever beam experiment including their classification into matrix cracking, interfacial failure and fiber breakage are shown. Details of the experimental setup are found in [Sause, 2010d, Sause, 2012b], while references [Sause, 2010c, Sause, 2012a] focus on the underlying methodology. The black data points are the resulting feature values of the current simulation work with black circles marking the signals propagation direction. For the current evaluation along one propagation direction, the feature range observed is quite comparable to the typical extent of one cluster observed for a particular failure mechanism (i.e. matrix cracking, interfacial failure or fiber breakage). Thus, the presence of a failure type, as modeled herein, is expected to increase the dimensions of the cluster belonging to a particular failure type.

## 6. Conclusions

Within this study the influence of internal damage in fiber-reinforced composites on signal propagation of Lamb waves was investigated. For the present study a unidirectional fiber-reinforced plate was studied, including embedded models for inter-fiber cracks, broken fibers and inter-ply delamination located in the 0° direction of the plate.

Overall, a significant influence on the signals from all damage types was observed that is well detectable with piezoelectric sensors, and thus a feasible approach for SHM utilizing guided wave monitoring.



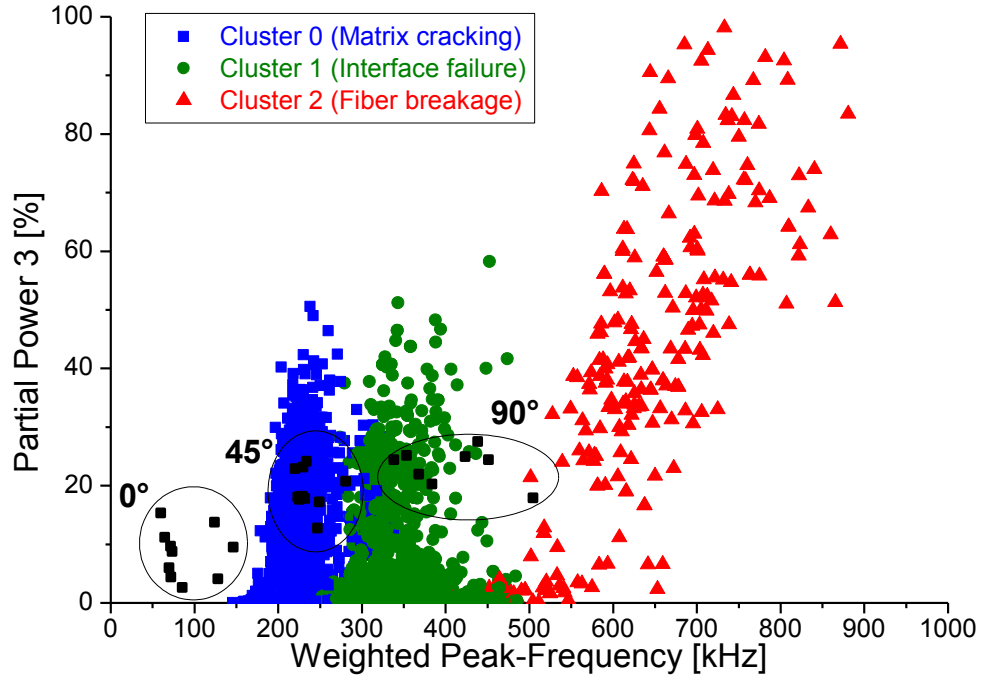


Fig. 15. Diagram of weighted peak frequency vs. partial power 3 of experimental measurement of double cantilever beam specimen [Sause, 2010d] compared to positions of features extracted from simulated signals for 0°, 45° and 90° propagation direction (all configurations).

For AE analysis, the largest impact is expected for source localization routines, since the internal damage types can act as virtual AE source caused by modal conversion effects. This significantly alters the emitted wave field of the original source and may even affect the initial arrival time of the different wave modes, causing substantial errors during source localization.

Also, energetic features and frequency features extracted from the Lamb-wave signals are influenced by the presence of internal damage. In some configurations, the influence on a particular feature value was found to be very significant. However, the overall range of values of the extracted features is comparable to ranges where pattern recognition approaches still can lead to valid classifications of source mechanisms. In contrast, the evaluation of signals with different observation angles relative to the source positions might cause a larger impact with respect to the accuracy of pattern recognition methods.

## Acknowledgment

I would like to thank Marvin A. Hamstad for the possibility to discuss AE sensing technologies and signal propagation in fiber-reinforced polymers.

## Literature

- [Castaings, 2004] M. Castaings, C. Bacon, B. Hosten and M. V. Predoi (2004), J. Acoust. Soc. Am., 115:3, 1125-1133.
- [Choi, 1989] H. Choi, W. Williams, IEEE Transactions on Acoustics, Speech and Signal Processing, 37:6, 862-872.

- [Gary, 1994] J. Gary and M. A. Hamstad (1994), J. Acoustic Emission, 12:3-4, 157-170.
- [Hamstad, 2002] M.A. Hamstad, A. O’Gallagher, J. Gary, J. Acoustic Emission, 12:3-4, 157-170.
- [Hamstad, 2008] M.A. Hamstad, J. Acoustic Emission, 26, 40-59.
- [Lamb, 1917] H Lamb, ‘On Waves in an Elastic Plate’, Proceedings of the Royal Society of London Series A Containing Papers of a Mathematical and Physical Character, Vol 93, pp 114-128, 1917.
- [Lowe, 1995] M. Lowe, IEEE Transactions on Ultrasonics Ferroelectrics and Frequency Control, 42:4, 525-542.
- [Raghavan, 2007] A. Raghavan, C. Cesnik, The Shock and Vibration Digest, 39, 91-114.
- [Sause, 2010a] M. G. R. Sause and S. Horn (2010), J. Nondest. Eval., 29:2, 123-142.
- [Sause, 2010b] M. G. R. Sause and S. Horn (2010), J. Acoustic Emission, 28, 142-154.
- [Sause, 2010c] M. G. R. Sause (2010), Identification of failure mechanisms in hybrid materials utilizing pattern recognition techniques applied to acoustic emission analysis, PhD-thesis, mbv-Verlag, Berlin.
- [Sause, 2010d] M. G. R. Sause and S. Horn, Influence of Specimen Geometry on Acoustic Emission Signals in Fiber Reinforced Composites: FEM-Simulations and Experiments, 29<sup>th</sup> European Conference on Acoustic Emission Testing, Vienna 09/2010
- [Sause, 2012a] M.G.R. Sause, A. Gribov, A.R. Unwin, S. Horn, Pat. Rec. Letters, 33:1, 17-23.
- [Sause, 2012b] M.G.R. Sause, T. Müller, A. Horoschenkoff, S. Horn, Comp. Sci. Technol., 72, 167-174.
- [Sause, 2012c] M.G.R. Sause, M.A. Hamstad, S. Horn, Sens. Act. A., 184, 64-71.
- [Sause, 2012d] M. G. R. Sause, S. Horn, Influence of Internal Discontinuities on Ultrasonic Signal Propagation in Carbon Fiber Reinforced Plastics, 30<sup>th</sup> European Conference on Acoustic emission Testing, Granada 09/2012
- [Wang, 2007] L. Wang, F. Yuan, Comp. Sci. Technol., 67, 1370-1384.
- [Zeyede, 2010] R. Zeyede, Notes on orthotropic Lamb waves, Technion - Israel Institute of Technology, <http://mercurial.intuxication.org/hg/elasticssim/>